Electrochimica Acta 536 (2025) 146746

Contents lists available at ScienceDirect

Electrochimica Acta

journal homepage: www.journals.elsevier.com/electrochimica-acta

# Annealing condition engineering of electrospun iron-titanium oxide nanofibers for enhanced lithium storage performance

Lisha Zhang [a,1], Fei Xie [a,1], Shujin Hao [a], Feiyu Diao [b,*], Yiqian Wang [a,*]

[a] College of Physics, Qingdao University, No 308 Ningxia Road, Qingdao, 266071, China
[b] Industrial Research Institute of Nonwovens & Technical Textiles, Shandong Center for Engineered Nonwovens, College of Textiles & Clothing, Qingdao University, No 308 Ningxia Road, Qingdao, 266017, China

ARTICLE INFO

*Keywords:*
Lithium-ion batteries
Iron/titanium-based oxide compounds
Electrospinning
Annealing condition
Electrochemical performance

ABSTRACT

Iron/titanium-based oxide compounds have garnered significant attention for their promising applications in lithium-ion batteries. To implement this, a large-scale fabrication technique such as electrospinning has become pivotal for the preparation of one-dimensional iron/titanium-based oxide nanocomposites. However, there exists a notable gap in understanding the influence of annealing conditions on the structure, morphology and electrochemical properties of resultant products. In this work, iron-titanium-based oxide nanofibers are produced *via* electrospinning followed by subsequent annealing, and the influence of annealing atmospheres on the products is systematically investigated. When annealed at 600 °C in an argon atmosphere, the product is carbon nanofibers loaded with $FeTiO_3$ and $Fe_3O_4$ nanoparticles ($FeTiO_3$/$Fe_3O_4$/CNFs), while annealing in air the product is carbon nanofibers embedded with $Fe_2TiO_5$ nanoparticles ($Fe_2TiO_5$/CNFs). Electrochemical tests demonstrate that $FeTiO_3$/$Fe_3O_4$/CNFs maintain a capacity of 395.6 mAh $g^{-1}$ after 100 cycles at a current density of 0.2 A $g^{-1}$, which is higher than that of $Fe_2TiO_5$/CNFs (174 mAh $g^{-1}$) and $Fe_3O_4$/CNFs (314 mAh $g^{-1}$). Moreover, $FeTiO_3$/$Fe_3O_4$/CNFs present a remarkable rate capability, possessing a capacity of 212.1 mAh $g^{-1}$ at 2.0 A $g^{-1}$. This excellent performance is attributed to the synergistic effect between $FeTiO_3$ and $Fe_3O_4$ and buffering effect of the carbon fibers. These findings highlight the significant application potential of iron/titanium oxides in the field of electrochemical energy storage.

## 1. Introduction

Iron/titanium (Fe/Ti) oxides have emerged as highly promising anode materials for lithium-ion batteries (LIBs), owing to their relatively high theoretical specific capacity, i.e., $FeTiO_3$ (530 mAh $g^{-1}$) and $Fe_2TiO_5$ (810 mAh $g^{-1}$) [1,2]. These oxides hold great potential for advancing the performance of LIBs, which are crucial for a wide range of applications including portable electronics, electric vehicles, and energy storage systems. However, despite of their attractive properties, Fe/Ti oxides often suffer from notable issues such as capacity fading, volume expansion, and pulverization during charge-discharge cycles, which negatively affect their cycling stability and limit their practical applications [3,4]. Addressing these challenges is essential for improving the performance of Fe/Ti-based LIBs.

To enhance the cycling stability of Fe/Ti oxides, researchers have tried various strategies, such as fabrication of one-dimensional (1D) nanostructures [5] and incorporation of carbon materials [6,7], particularly carbon fibers. For instance, Lian et al. [8] reported that $Fe_2TiO_5$ nanochains maintained a full retention of their initial specific capacity after 1000 cycles at a current density of 1.0 A $g^{-1}$, thereby confirming a significant enhancement in cycling stability offered by the unique chain morphology. In addition, Xia et al. [9] reported a high discharge capacity of 494.5 mAh $g^{-1}$ for $TiO_2$-$Fe_2TiO_3$@carbon nanocomposites after 150 cycles at a current density of 0.1 A $g^{-1}$. These results underscore the synergistic effect of combining one-dimensional nanostructures with carbon coating strategies in the Fe/Ti-based oxide composites. The aligned morphology facilitates charge transfer kinetics while the carbon layer enhances structural integrity during prolonged cycling, collectively contributing to improved electrochemical durability.

Electrospinning followed by subsequent annealing offers a promising method for fabricating 1D carbon-coated metal oxide composites. This method involves two crucial stages: spinning and annealing. During the

* Corresponding authors.
*E-mail addresses:* fydiao@qdu.edu.cn (F. Diao), yqwang@qdu.edu.cn (Y. Wang).
[1] These authors contributed to this work equally.

https://doi.org/10.1016/j.electacta.2025.146746
Received 29 March 2025; Received in revised form 10 June 2025; Accepted 21 June 2025
Available online 21 June 2025

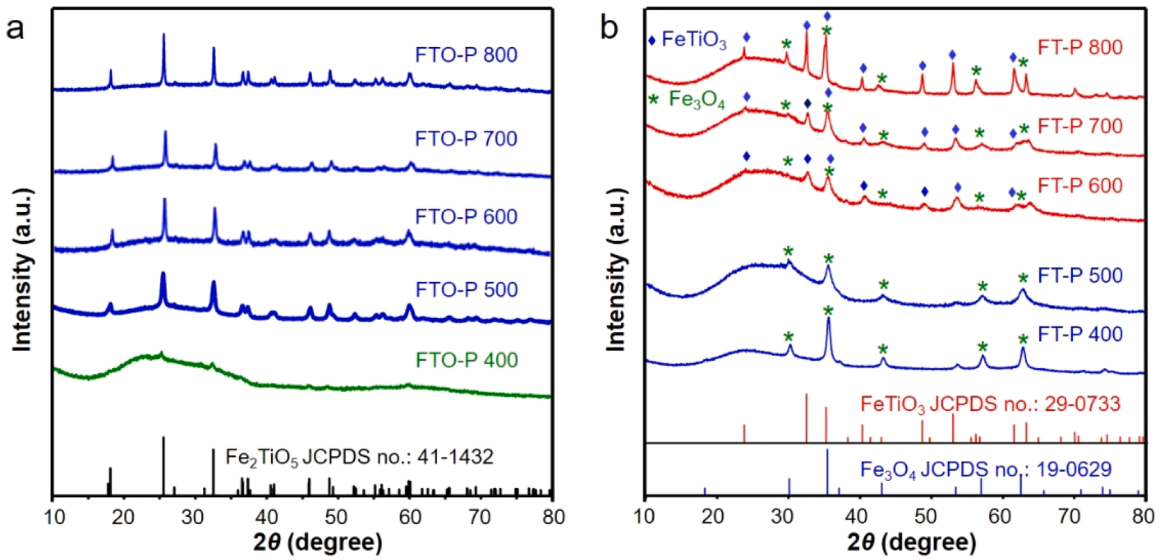


**Fig. 1.** XRD patterns of the FTO-P 400–800 (a) and FT-P 400–800 (b).

spinning process, a solution is electrospun into a fibrous membrane. Subsequently, the metal salts in the fibers are calcined into metal oxides during the annealing process. Numerous studies have focused on the effects of the spinning solution composition and electrospinning process parameters on the final products [10–13]. However, the influence of different annealing conditions on the morphology, structure, and electrochemical properties of the resultant products remains unexplored. Hence, it is necessary to carry out a comprehensive investigation on the effect of annealing process.

In this work, the influence of annealing conditions on the electrospun Fe/Ti-based oxide nanofibers was systematically investigated. Different Fe/Ti-based oxide nanofibers were prepared by adjusting the annealing atmosphere. $FeTiO_3/Fe_3O_4$/CNFs were obtained by annealing at 600 °C in an argon atmosphere, while $Fe_2TiO_5$/CNFs were produced at the same temperature but in an air atmosphere, highlighting the critical role of the annealing atmosphere. $FeTiO_3/Fe_3O_4$/CNFs exhibited enhanced cycling stability and rate performance than $Fe_2TiO_5$/CNFs, which is attributed to the synergistic effect between $FeTiO_3$ and $Fe_3O_4$ and buffering effect of the carbon fibers.

## 2. Experimental

### 2.1. Materials

Polyvinylpyrrolidone (PVP, average Mw ~1300,000) with a purity of 99.5 % serves as the carbon sources. The Fe and Ti sources come from ferric acetylacetonate [$Fe(acac)_3$, 98 %] and tetrabutyl titanate [$Ti(C_4H_9O)_4$, 99.5 %], respectively. The solvents are ethanol ($CH_3CH_2OH$) and acetic acid ($CH_3COOH$), both with a purity of 99.5 %, provided by Sinopharm Group Chemical Reagent Company Limited. All the chemicals have not undergone further purification.

### 2.2. Synthesis of the fiber membranes

First, $Fe(acac)_3$ and $Ti(C_4H_9O)_4$ were mixed in a molar ratio of 2:1 and added into a solution of acetic acid and ethanol (1:1 vol ratio) containing 10 wt. % PVP. The mixture was stirred thoroughly until dissolved. Next, the spinning solution was drawn into a disposable needle for electrospinning. The spinning conditions were set as follows: a voltage of 16 kV, a needle-to-collector distance of 16 cm, a feed rate of 0.33 mL/h, and a roller collector speed of 550 rpm. The electrospinning process was conducted at room temperature with a relative humidity of 33–36 %. After spinning, the fiber membrane was placed in a tubular furnace and annealed in argon or air, at a heating rate of 2 °C/min, with an annealing temperature range from 400 °C to 800 °C and an annealing time of 6 h. The products obtained from annealing in argon and air were labeled as FT-P 400–800 and FTO-P 400–800, respectively.

### 2.3. Materials characterization

The crystal structures of as-prepared fiber membranes were investigated using an X-ray diffractometer (XRD, Rigaku) with Cu-$K_\alpha$ radiation ($\lambda = 1.5406$ Å). Their morphologies were studied using a field-emission scanning electron microscope (FE-SEM, Sigma 500) at an accelerating voltage of 20 kV. The nitrogen adsorption-desorption tests were carried out on an automatic volumetric sorption analyzer (NOVA 1100, Quantachrome, USA) at 77 K. The Brunauer-Emmett-Teller (BET) method was used to calculate the specific surface area and total pore volume of the products. The Barrett-Joyner-Halenda (BJH) method was utilized to obtain the pore size distribution from the desorption branches of the isotherms. The chemical compositions of the fiber membranes were determined using an energy dispersive X-ray spectrometer (EDS, Oxford INCAx Sight6427). The valence states of the elements in the fiber membranes were determined by X-ray photoelectron spectroscopy (XPS, Thermo Scientific K-Alpha$^+$). Bright-field (BF), selected area electron diffraction (SAED) and high-resolution transmission electron microscopy (HRTEM) images were obtained using a transmission electron microscope (TEM, JSM-2100Plus) at 200 kV. Thermogravimetric analysis (TGA) was carried out on thermogravi metric apparatus (TG209F3, NETZSCH, Germany) at temperatures ranging from 40° to 900 °C with a heating rate of 10 °C/min.

### 2.4. Electrochemical measurements

The annealed fiber membranes were used as anode materials for LIBs and their lithium storage capacity were investigated. At the same time, the weight of each electrode was measured to calculate the mass of the active substance. A mixture of 1 M $LiPF_6$ solution and ethylene carbonate (EC)/dimethyl carbonate (DMC)/diethyl carbonate (DEC) (1:1:1 vol ratio) was used as electrolyte and a lithium foil was used as the counter electrode. The assembly of CR2025 button battery was performed in a high-purity argon filled glove box with moisture and oxygen kept below 0.1 ppm. The rate performance and cycling stability were tested using a LAND CT2001 battery test system with a voltage range of 0.01–3.00 V. Cyclic voltammetry (CV) and electrochemical impedance spectroscopy (EIS) tests were carried out on a Metrohm Autolab

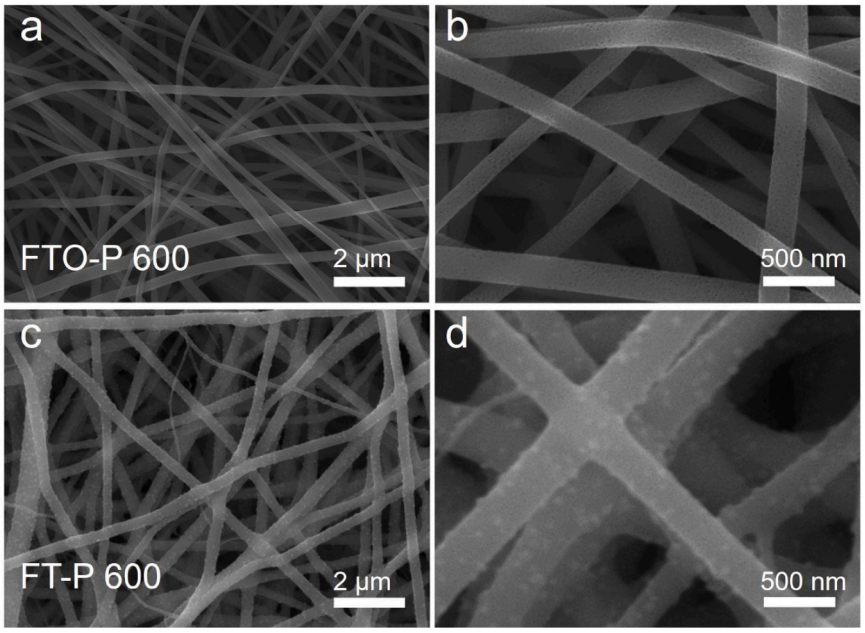


**Fig. 2.** (a) Low-magnification and (b) high-magnification FE-SEM images of FTO-P 600, (c) low-magnification and (d) high-magnification FE-SEM images of FT-P 600.

electrochemical workstation (PGSTAT 302 N). CV curves were obtained at a scan rate of 0.3 mV $s^{-1}$ over a potential range of 0.01–3.00 V. EIS spectra were recorded at a disturbance amplitude of 5 mV with the frequency range from 100 kHz to 0.01 Hz.

## 3. Results and discussion

Fig. 1a presents the XRD patterns of the products (FTO-P 400–800) annealed in air. The broad peak at 24° in the XRD pattern of FTO-P 400 indicates the presence of amorphous carbon. In the XRD patterns of FTO-P 500–800, this broad peak can not be obviously observed. The other diffraction peaks in the XRD patterns of FTO-P 400–800 can be indexed using the orthorhombic $Fe_2TiO_5$ (JCPDS no.: 41–1432, $a = 9.7965$ Å, $b = 9.9805$ Å, $c = 3.7301$ Å, $\alpha = \beta = \gamma = 90°$). TGA analysis (Fig. S1) shows that the quality loss curve of FTO begins to flatten out, when the temperature reaches 400 °C, which is caused by the decomposition of PVP and the formation of $Fe_2TiO_5$. The mass ratio of $Fe_2TiO_5$ and amorphous carbon in FTO-P 600 is determined to be 1:33 from the quantitative analysis of its XRD pattern. Fig. 1b shows the XRD patterns of FT-P 400–800. A broad diffraction peak at 24° is observed for all the samples, indicating the presence of amorphous carbon. Besides, for FT-P 400 and FT-P 500, additional diffraction peaks correspond to the cubic phase of $Fe_3O_4$ (JCPDS no.: 19–0629, $a = 8.396$ Å), suggesting that both FT-P 400 and FT-P 500 consist of amorphous carbon and $Fe_3O_4$. For the FT-P 600, diffraction peaks at 30.1°, 35.3°, 43.1°, 56.9° and 62.5° are observed, which correspond to the (220), (311), (400), (511) and (440) planes of $Fe_3O_4$, respectively [14]. In the FT-P 600, the diffraction peaks at 23.8°, 32.5°, 35.3°, 40.3°, 48.7°, 53.0° and 61.5° can correspond to the (012), (104), (110), (113), (024), (116) and (214) planes of hexagonal $FeTiO_3$ (JCPDS no.: 29–0733, $a = b = 5.0884$ Å, $c = 14.0930$ Å, $\alpha = \beta = 90°$, $\gamma = 120°$), respectively. This indicates the coexistence of amorphous carbon, $Fe_3O_4$ and $FeTiO_3$ in the FT-P 600. The mass ratio of $Fe_3O_4$, $FeTiO_3$ and amorphous carbon in the FT-P 600 is determined to be 1:26.5:11 from the quantitative analysis of its XRD pattern. The XRD patterns of FT-P 700 and FT-P 800 are similar to those of FT-P 600. Therefore, both FT-P 700 and FT-P 800 consist of amorphous carbon, $Fe_3O_4$ and $FeTiO_3$.

To explore the effects of different atmospheres on the microstructure and electrochemical properties of the products, we selected the products annealed at 600 °C for detailed analysis. From the low-magnification FE-SEM images (Fig. 2a and c) of FTO-P 600 and FT-P 600, it can be seen that fibers are well dispersed and have relatively uniform diameters. Specifically, the average diameter of FTO-P 600 is approximately 206 nm, whereas it is about 220 nm for FT-P 600. The enlarged SEM images of FTO-P 600 and FT-P 600 are presented in Fig. 2b and d, respectively. The fibers in FTO-P 600 display a relatively smooth surface, and their surface is covered with numerous fine pores. In contrast, numerous small nanoparticles are observed on the surface of the fibers in FT-P 600. The specific surface area and pore size distribution of FTO-P 600 and FT-P 600 were investigated through nitrogen adsorption-desorption tests, as shown in Fig. S2. Fig. S2 demonstrates hysteresis loops of type-IV adsorption/desorption isotherms, indicating that both samples exhibit a mesoporous nature. For the pore size range from 10 nm to 35 nm, both FTO-P 600 and FT-P 600 have a similar pore size distribution. However, for the pore size range from 4.5 nm to 10 nm, FTO-P 600 and FT-P 600 exhibit different behaviors.

Fig. 3a and b present FE-SEM images of FTO-P 600 and FT-P 600, along with the corresponding elemental mapping images for C, O, Fe and Ti. The associated EDS spectra are displayed in Fig. 3c and d. The inset tables show the mass ratios of the detected elements. Upon careful examination, it is found that C, O, Fe and Ti are uniformly distributed throughout an individual fiber of both FTO-P 600 and FT-P 600. Fe, O and Ti are dispersed more evenly in FTO-P 600 than in FT-P 600 because the nanoparticles in FT-P 600 are larger, whereas the C content is significantly lower in FTO-P 600 than in FT-P 600.

TEM examination was performed on FTO-P 600 and FT-P 600 to gain deeper insights into their structure and microstructure. Fig. 4a shows a BF TEM image of FTO-P 600, revealing a fibrous morphology. Fig. 4c presents a magnified image of the region enclosed by a red rectangle in Fig. 4b For the nanoparticles, the lattice spacings are measured to be 2.22 Å and 2.39 Å, with an interplanar angle of 83°, corresponding to the (240) and ($3\bar{1}1$) crystal planes of orthorhombic $Fe_2TiO_5$, respectively. Fig. 4d displays the SAED pattern of FTO-P 600, which can be indexed using the orthorhombic $Fe_2TiO_5$. These results collectively demonstrate that annealing in air at 600 °C yields carbon nanofibers loaded with $Fe_2TiO_5$ nanoparticles ($Fe_2TiO_5$/CNFs). For FT-P 600, the BF TEM image in Fig. 4e shows a fibrous structure decorated with nanoparticles. Fig. 4f presents the SAED pattern of FT-P 600, where the diffraction rings

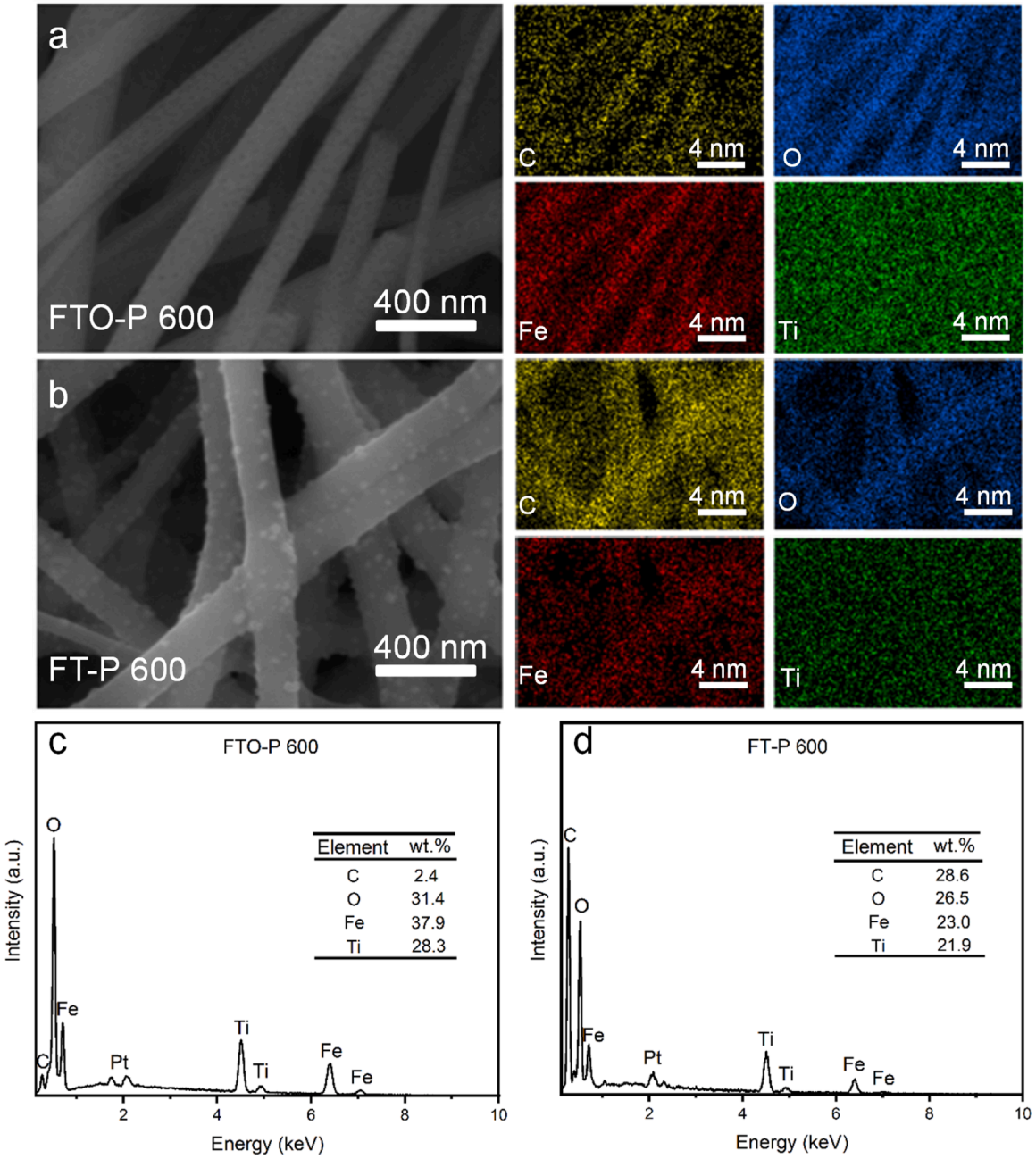


**Fig. 3.** (a) FE-SEM image of FTO-P 600 and its elemental mapping images related to C, O, Fe and Ti, (b) FE-SEM image of FT-P 600 and its elemental mapping images related to C, O, Fe and Ti, (c) EDS energy spectrum of FTO-P 600, (d) EDS energy spectrum of FT-P 600.

corresponding to $FeTiO_3$ and $Fe_3O_4$ are marked with white and red lines, respectively. From inner to outer, the diffraction rings can be indexed as (104), (113), (024) and (214) crystal planes for $FeTiO_3$, and (311) and (422) crystal planes for $Fe_3O_4$. Fig. 4g and 4h show HRTEM images of FT-P 600. The lattice spacing of 2.75 Å in Fig. 4g is consistent with the (104) plane of $FeTiO_3$, while the spacing of 2.53 Å in Fig. 4h corresponds to the (311) plane of $Fe_3O_4$. These findings confirm that the annealing at 600 °C in argon leads to the formation of carbon nanofibers loaded with $FeTiO_3$ and $Fe_3O_4$ nanoparticles ($FeTiO_3$/$Fe_3O_4$/CNFs).

The valence states of the elements in FTO-P 600 and FT-P 600 were investigated using XPS. Fig. 5a displays the full XPS spectrum of FTO-P 600, revealing characteristic peaks of Fe 2*p*, Ti 2*p* and O 1*s* , which confirm the presence of Fe, Ti and O in the FTO-P 600. Fig. 5c shows the high-resolution Fe 2*p* spectrum of FTO-P 600. The broad peaks at 711 eV and 724 eV correspond to the Fe $2p_{3/2}$ and Fe $2p_{1/2}$, respectively [15]. Additionally, the satellite peaks at 719 eV and 732 eV are indicative of $Fe^{3+}$ [16], confirming that iron in the FTO-P 600 exists predominantly in a trivalent state. Fig. 5e presents the high-resolution Ti 2*p* spectrum of FTO-P 600. The peaks at 458 eV and 464 eV are assigned to the Ti $2p_{3/2}$ and Ti $2p_{1/2}$, respectively, indicating the presence of $Ti^{4+}$ in the FTO-P 600 [17]. Fig. 5g shows the high-resolution O 1*s* spectrum of FTO-P 600. The peaks near 530 eV and 532 eV are attributed to the oxygen in the lattice and surface defect sites (e.g., adsorbed oxygen or hydroxyl groups), respectively [18,19]. The above results collectively verify that the Fe/Ti-based oxide in FTO-P 600 is $Fe_2TiO_5$. Fig. 5b displays the full XPS spectrum of FT-P 600. Fig. 5d shows the high-resolution Fe 2*p* spectrum of FT-P 600, with peaks at 711 eV and 725 eV corresponding to the Fe $2p_{3/2}$ and Fe $2p_{1/2}$, respectively. Peak deconvolution reveals two components for each orbital: the peaks at 710 eV and 724 eV are assigned to $Fe^{2+}$, while the peaks at 712 eV and 726 eV correspond to

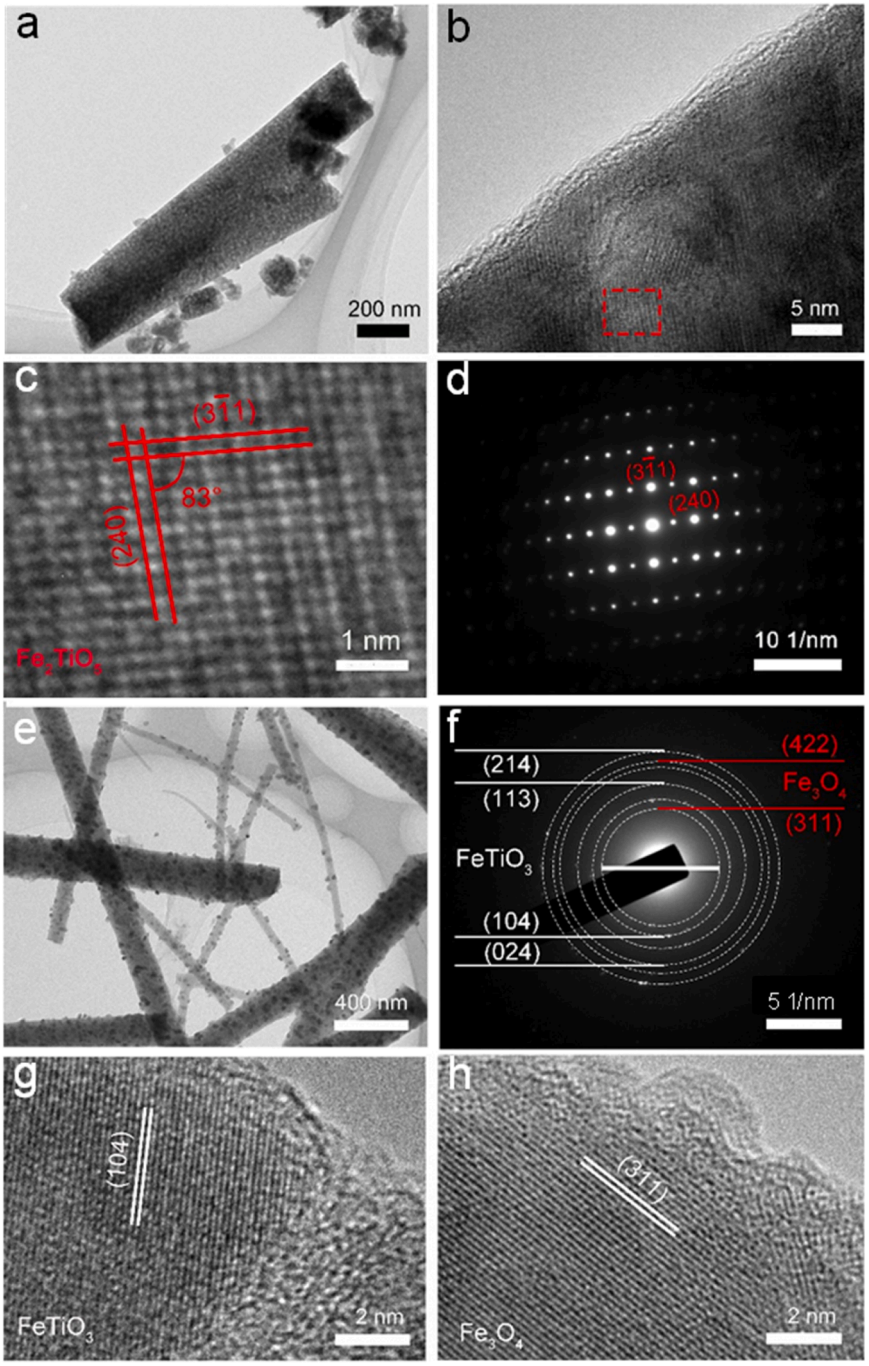


**Fig. 4.** (a) TEM bright field image of FTO-P 600, (b) HRTEM image of FTO-P 600, (c) enlarged image of the red rectangular area in (b), (d) SAED image of FTO-P 600, (e) TEM bright field image of FT-P 600, (f) SAED image of FT-P 600, (g and h) HRTEM images of FT-P 600.

$Fe^{3+}$. The satellite peak at 720 eV further proves the presence of $Fe^{2+}$ and $Fe^{3+}$ in the FT-P 600. Fig. 5f presents the high-resolution Ti 2*p* spectrum of FT-P 600, with peaks at 458 eV and 464 eV corresponding to the Ti $2p_{3/2}$ and Ti $2p_{1/2}$, respectively [20]. The shoulder peak near 456 eV corresponds to $Ti^{3+}$ [17], which is due to the fact that the $Ti^{3+}$ intermediate is not completely oxidized in argon atmosphere, resulting in existence of mixed valence states ($Ti^{4+}$/$Ti^{3+}$) in the FT-P 600. Fig. 5h shows the high-resolution O 1*s* spectrum of FT-P 600, where the peaks at 530 eV and 532 eV are attributed to oxygen in the lattice and surface defect sites, respectively. Combined with the XRD results, it is confirmed that the Fe/Ti-based oxides in FT-P 600 consist of $FeTiO_3$ and $Fe_3O_4$.

To investigate the electrochemical performance of FTO-P 600 and FT-P 600 as anode materials for lithium-ion batteries, electrochemical tests were systematically conducted. Fig. 6a presents the initial six CV curves of FTO-P 600 in the voltage range of 0.01–3.00 V (vs. Li) at a scan rate of 0.3 mV $s^{-1}$. During the first cathodic process, three distinct reduction peaks emerge at 1.6 V, 1.2 V and 0.3 V. The peak at 1.6 V corresponds to the phase decomposition of $Fe_2TiO_5$ into $Fe_2O_3$ and $TiO_2$ accompanied by $Li^+$ intercalation into the $TiO_2$ lattice [21]. Concurrently, the peak at 1.2 V corresponds to the $Li^+$ insertion into the $Fe_2O_3$ matrix, whereas the peak at 0.3 V signifies the formation of the solid electrolyte interface (SEI) film, metallic iron and $Li_2O$ [21]. In the subsequent cycle, the reduction peaks at 1.6 V, 1.2 V and 0.3 V disappear, and a new reduction peak appears at 0.7 V, corresponding to the reduction reaction of the $Fe_2TiO_5$. This indicates that the decomposition of $Fe_2TiO_5$ is irreversible [22–24]. During the initial anodic process, two

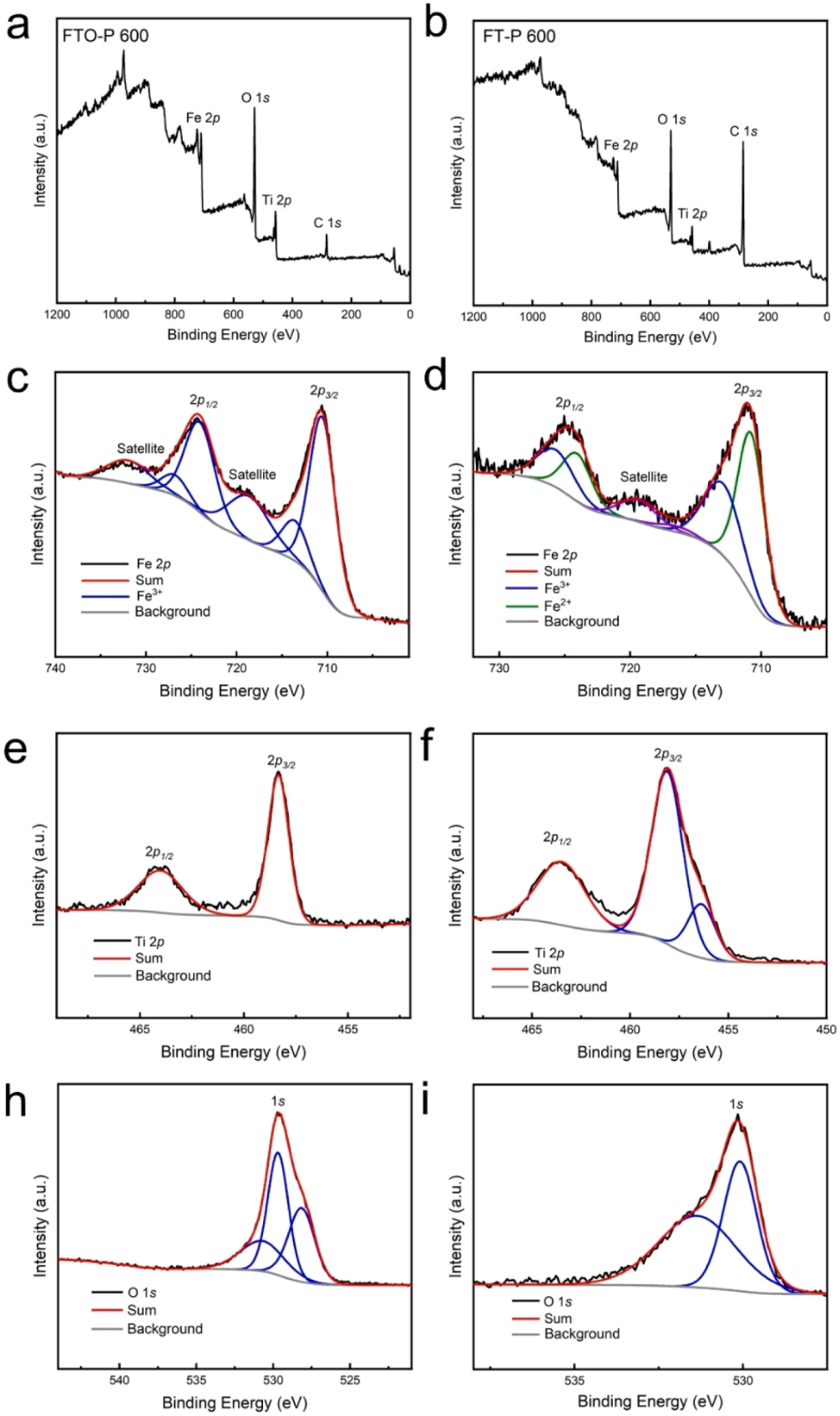


**Fig. 5.** XPS spectrum of FTO-P 600: (a) XPS full spectrum, (c) XPS spectrum of Fe 2*p*, (e) XPS spectrum of Ti 2*p*, (g) XPS spectrum of O 1*s* ; XPS spectrum of FT-P 600: (b) XPS full spectrum, (d) XPS spectrum of Fe 2*p*, (f) XPS spectrum of Ti 2*p*, (h) XPS spectrum of O 1*s* .

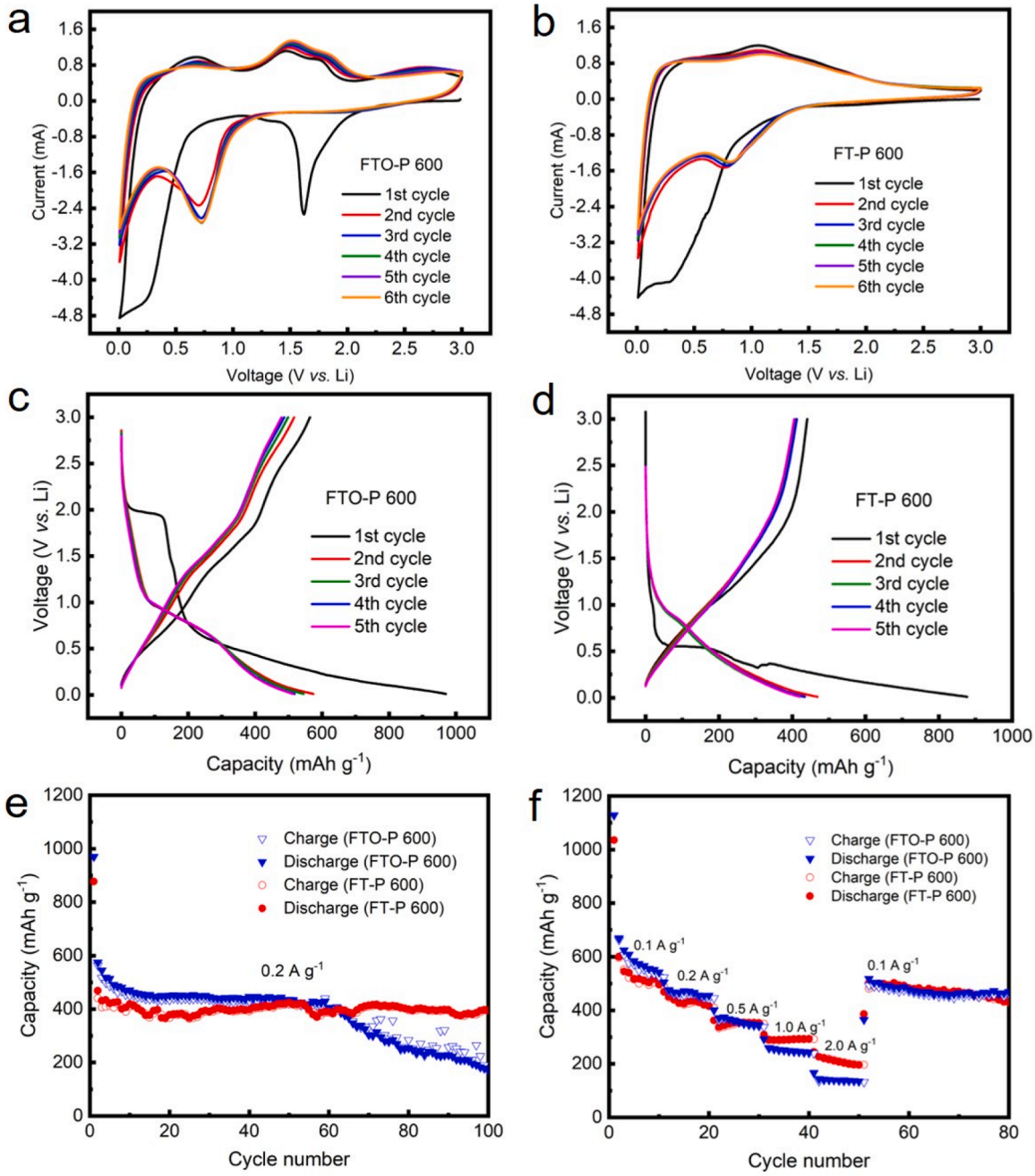


**Fig. 6.** CV curves of (a) FTO-600 and (b) FT-P 600 obtained at 0.3 mV $s^{-1}$, voltage versus capacity curves of (c) FTO-P 600 and (d) FT-P 600 electrodes at 0.2 A $g^{-1}$, (e) rate performance of at different current densities, (f) cycling performance at 0.2 A $g^{-1}$.

characteristic oxidation peaks are demonstrated. The peak at 1.5 V represents the extraction of $Li^+$from both $TiO_2$ and $Fe_2O_3$ lattices, while the peak at 1.8 V corresponds to metallic iron oxidation ($Fe^0 \rightarrow Fe^{3+}$) accompanied by $Li^+$ deintercalation [25]. The electrochemical reactions are displayed as follows [20,21].

$$Fe_2TiO_5 + x\ Li^+ + xe^- \rightarrow Fe_2O_3 + Li_xTiO_2 \quad (1)$$

$$Fe_2O_3 + x\ Li^+ + xe^- \rightarrow Li_xFe_2O_3 \quad (2)$$

$$Li_xFe_2O_3 + (6\text{-}x)\ Li^+ + (6\text{-}x)e^- \rightarrow 3Li_2O + 2Fe \quad (3)$$

For the FT-P 600 electrode, the initial six CV curves in Fig. 6b reveal distinct electrochemical signatures, with initial cathodic peaks at 0.3 V (formation of SEI film) and 0.6 V (intercalation of $Li^+$ and reduction of $Fe^{3+}/Fe^{2+}$ to $Fe^0$), and an anodic peak at 1.1 V (oxidation of $Fe^0$). In subsequent redox cycles, the reduction peak shifts from 0.6 V to 0.8 V, accompanied by a rightward shift of the corresponding oxidation peak. The overlap in the CV curves beyond the second cycle demonstrates an excellent cycling stability of FT-P 600. The electrochemical reactions governing these processes can be summarized as follows [26–29].

$$FeTiO_3 + (2 + x)Li^+ + (2 + x)e^- \rightarrow Fe^0 + Li_xTiO_2 + Li_2O \quad (4)$$

$$Fe_3O_4 + 8Li^+ + 8e^- \rightarrow Fe^0 + 4Li_2O \quad (5)$$

$$Li_xTiO_2 + Fe + Li_2O \rightarrow FeO + TiO_2 + (2 + x)Li^+ + (2 + x)e^- \quad (6)$$

$$Fe^0 + 4Li_2O \rightarrow Fe_3O_4 + 8Li^+ + 8e^- \quad (7)$$

Figs. 6c and 6d illustrate the initial five discharge/charge profiles of FTO-P 600 and FT-P 600 electrodes at a current density of 0.2 A $g^{-1}$. The

**Table 1**
Cycling and rate performances of the FT-P 600 electrode and the iron/titanium oxide electrodes reported in the literature.

| Sample | Cycling performance | | | Rate performance | | Ref. |
|---|---|---|---|---|---|---|
| | Current density (A $g^{-1}$) | Cycle number | Capacity (mAh $g^{-1}$) | Current density (A $g^{-1}$) | Capacity (mAh $g^{-1}$) | |
| $Fe_2TiO_5$ | 0.1 | 100 | 355.1 | 0.1 | 406.2 | [32] |
| | | | | 3.2 | 76.6 | |
| $Fe_2TiO_5$ | 0.036 | 50 | 151.3 | — | | [33] |
| $Fe_2TiO_5$ | 0.5 | 250 | 234.1 | 0.1 | 363.7 | [23] |
| | | | | 1.6 | 117.5 | |
| $Fe_2TiO_5$ | — | | | 0.1 | 500.0 | [8] |
| | | | | 5.0 | 180.0 | |
| FT-P 600 | 0.2 | 100 | 395.6 | 0.1 | 578.1 | This work |
| | | | | 2.0 | 212.1 | |

charge-discharge plateaus align well with the redox peaks observed in the CV curves, confirming the consistency of the electrochemical behavior. The initial discharge specific capacities of FTO-P 600 and FT-P 600 electrodes are 969.7 and 877.3 mAh $g^{-1}$, respectively. In the FT-P 600, $Fe_3O_4$ (2.6 wt. %) contributes 0.9 % of the whole capacity; $FeTiO_3$ (69.0 wt. %) provides approximately 21.2 % of the capacity; 77.9 % of the whole capacity comes from the carbon nanofibers. In the FTO-P 600, $Fe_2TiO_5$ (97.1 wt. %) offers 78.7 % of the total capacity, and carbon nanofibers afford 21.3 % of the whole capacity. To further explore the electrochemical performance of FTO-P 600 and FT-P 600, the rate performance and cycling stability were examined. Fig. 6e illustrates the cycling performance of two electrodes over 100 cycles at 0.2 A $g^{-1}$. The FT-P 600 electrode maintains a specific capacity of 395.6 mAh $g^{-1}$ after 100 cycles, which is higher than that of FTO-P 600 electrode. The specific capacity of the FT-P 600 electrode during the charging and discharging processes first decreases and then increases, which is due to the occurrence of irreversible reactions and the gradual activation of the electrode material as the cycle number increases. Fig. 6f reveals the rate performance of the two electrodes at different current densities. The FT-P 600 electrode delivers an excellent rate performance with average discharge capacities of 578.1, 434.6, 351.7, 293.6 and 212.1 mAh $g^{-1}$ at current densities of 0.1, 0.2, 0.5, 1.0 and 2.0 A $g^{-1}$, respectively. Notably, when the current density returns to 0.1 A $g^{-1}$, the capacity recovers to 484.7 mAh $g^{-1}$. Comparative analysis indicates that FT-P 600 exhibits better cycling stability and rate performance than FTO-P 600. This improvement can be attributed to the synergistic effect between $Fe_3O_4$ and $FeTiO_3$, as well as the buffering effect of carbon fibers, which optimize the structural stability and improve electrical conductivity [30,31]. Table 1 compares the cycling and rate performances of the FT-P 600 electrode with those reported in the literature for Fe/Ti oxide electrodes. From Table 1, it can be seen that the FT-P 600 electrode exhibits superior cycling stability and rate performance.

EIS tests were performed to investigate the electrochemical reaction kinetics of FTO-P 600 and FT-P 600 electrodes. Fig. 7a displays the EIS spectra and the fitting equivalent circuit of two electrodes. In the high-frequency region, the semicircle diameter represents the charge transfer resistance ($R_{ct}$). The $R_{ct}$ values of FTO-P 600 and FT-P 600 electrodes are 177.0 Ω and 136.0 Ω, respectively. The electrolyte impedance ($R_s$) is denoted by the impedance at the starting point of the semicircle. The $R_s$ values of FTO-P 600 and FT-P 600 electrodes are 1.1 Ω and 1.9 Ω, respectively. These results indicate that the FT-P 600 electrode exhibits lower charge transfer resistance and superior conductivity. Fig. 7b shows the fitting diagram of $Z_{re}$ and $\omega^{-0.5}$ for the FTO-P 600 and FT-P 600 electrodes. The inclined line in the low-frequency region of the EIS spectrum is related to the $Li^+$ diffusion coefficient ($D_{Li}$) of the electrode. $D_{Li}$ can be calculated using the following equations [34,35].

$$D_{Li} = \frac{R^2T^2}{2A^2n^4F^4C^2\sigma^2} \quad (8)$$

$$Z' = R_s + R_{ct} + \sigma\omega^{-0.5} \quad (9)$$

Where $A$ (electrode area) is 1.54 × $10^{-4}$ $m^2$, $R$ (gas constant) is 8.314 J $k^{-1}$ $mol^{-1}$, $F$ (Faraday constant) is 96,485 C $mol^{-1}$, $T$ is 298.15 K, $n$ is the number of electrons converted per mole of matter and $C$ is the concentration of lithium ions. Fig. 7b shows the relationship between $Z_{re}$ and $\omega^{-0.5}$, and the σ of the FTO-P 600 and FT-P 600 electrodes are 114.1 and 57.4 Ω $s^{-0.5}$, respectively. The calculated $D_{Li}$ values for FTO-P 600 and FT-P 600 electrodes are 1.9 × $10^{-17}$ $cm^2$ $s^{-1}$ and 1.6 × $10^{-14}$ $cm^2$ $s^{-1}$, respectively, indicating that the FT-P 600 electrode has a higher $Li^+$ diffusion ability [36].

To further verify the synergistic effect of $FeTiO_3$ and $Fe_3O_4$, the electrochemical performance of the FT-P 500 is compared with that of the FT-P 600. From the aforementioned XRD analysis, it shows that FT-P 500 consists of amorphous carbon and $Fe_3O_4$, while FT-P 600 is composed of amorphous carbon, $Fe_3O_4$ and $FeTiO_3$. A comprehensive analysis of the morphology, composition and microstructure of FT-P 500 was conducted, and detailed morphology and structural characterization of FT-P 500 is provided in the supporting information. Fig. 8a shows the CV curves of the first six cycles of FT-P 500 at a scan rate of 0.3 mV $s^{-1}$. During the first cathodic scan process, three reduction peaks at 0.3 V, 0.6 V and 1.0 V can be observed. The peak at 0.3 V corresponds to the formation of the SEI film, and the peak at 0.6 V is assigned to the

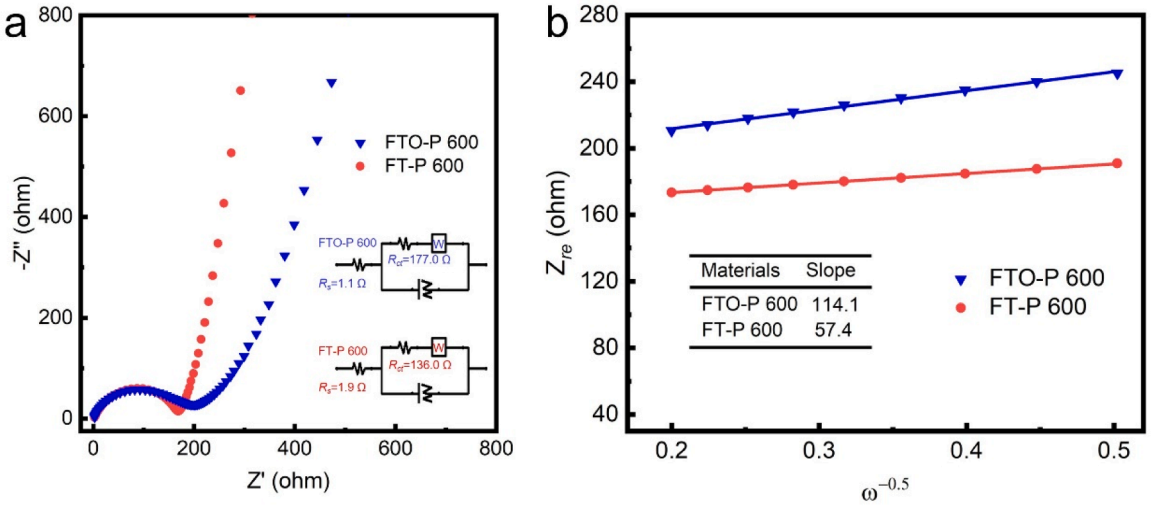


**Fig. 7.** (a) EIS spectra of FTO-P 600 and FT-P 600 electrodes, (b) graph of $Z_{re}$ plotted against $\omega^{-0.5}$.

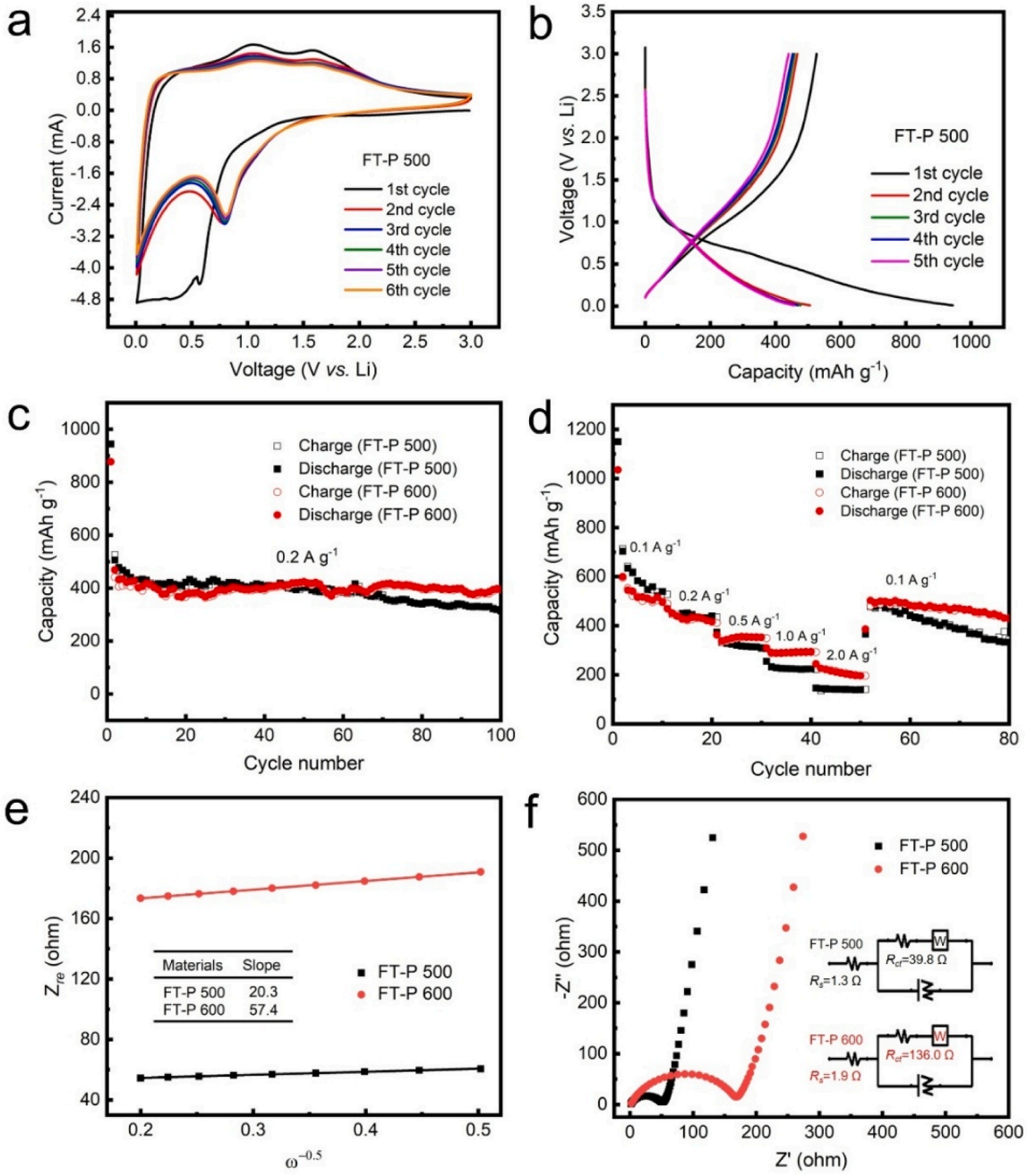


**Fig. 8.** CV curves of FT-P 500 (a) obtained at 0.3 mV $s^{-1}$, (b) the charge-discharge curves for the first five cycles, (c) cycling performance at a current density of 0.2 A $g^{-1}$, (d) rate performance at different current densities, (e) graph of $Z_{re}$ plotted against $\omega^{-0.5}$, (f) EIS spectra of FT-P 500 and FT-P 600 electrodes.

formation of $Fe^0$ and $Li_2O$ [37], while the peak at 1.0 V corresponds to the insertion of $Li^+$ into the $Fe_3O_4$ lattice [38]. In the initial anodic scan process, two peaks at 1.0 V and 1.6 V correspond to the oxidation of $Fe^0$ to $Fe^{2+}$ and $Fe^{3+}$, respectively [39]. In the subsequent redox process, a peak appears at 0.8 V, which corresponds to the reversible reduction of iron oxides [40]. The CV curves after the second cycle are highly overlapped, indicating that FT-P 500 has an excellent cycling stability. The electrochemical reactions governing these processes can be summarized as follows [37,38].

$$Li_xFe_3O_4 + (8–x)Li^+ + (8–x)e^- \rightarrow Fe^0 + 4Li_2O \quad (10)$$

$$Fe_3O_4 + xLi^+ + xe^- \rightarrow Li_xFe_3O_4 \quad (11)$$

Fig. 8b shows the initial five discharge/charge profiles of FT-P 500 electrode at 0.2 A $g^{-1}$. The charge-discharge plateaus align well with the redox peaks observed in the CV curves, confirming the consistency of the electrochemical behavior. At a current density of 0.2 A $g^{-1}$, the cycling performances of FT-P 500 and FT-P 600 electrodes are shown in Fig. 8c. It can be seen that the FT-P 600 electrode maintains a specific capacity of 395.6 mAh $g^{-1}$ after 100 cycles, higher than that of the FT-P 500 electrode. Fig. 8d demonstrates the rate performance of FT-P 500 and FT-P 600 electrodes at different current densities. It can be seen that the rate performance of the FT-P 600 is better than that of the FT-P 500. Fig. 8e is the fitting diagram of $Z_{re}$ and $\omega^{-0.5}$ of FT-P 500 and FT-P 600 electrodes. Using Equ. (1) and (2), the $D_{Li}$ is calculated to be $1.1 \times 10^{-15}$ and $1.6 \times 10^{-14}$ $cm^2$ $s^{-1}$ for FT-P 500 and FT-P 600 electrodes, respectively. The FT-P 600 electrode has a higher lithium-ion diffusion capacity, which is possibly due to the shortened diffusion path of $Li^+$ caused by the reduction of fiber diameter. Fig. 8f is the EIS spectra of FT- P 500 and FT-

P 600 electrodes. The corresponding equivalent circuit diagrams are shown in the inset of Fig. 8f. After fitting in the high-frequency region, for the FT-P 500 and FT-P 600 electrodes, the $R_{ct}$ values are 39.8 Ω and 136.0 Ω, and the $R_s$ values are 1.3 Ω and 1.9 Ω, respectively. The above analysis reveals that the FT-P 600 electrode has better cycling and rate performances than FT-P 500 electrode, which is ascribed to the synergistic effect between $FeTiO_3$ and $Fe_3O_4$ in FT-P 600.

## 4. Conclusions

In summary, we have systematically investigated the influence of annealing conditions on the structure, morphology and electrochemical properties of electrospun Fe/Ti-based oxide nanofibers. Two different atmospheres, air and argon, are chosen for the annealing process. When annealing at 600 °C in argon, $FeTiO_3/Fe_3O_4$/CNFs are produced; when annealing at 600 °C in air, $Fe_2TiO_5$/CNFs are obtained. It reveals that $FeTiO_3/Fe_3O_4$/CNFs exhibit superior cycling stability and rate performance compared to $Fe_2TiO_5$/CNFs and $Fe_3O_4$/CNFs. $FeTiO_3/Fe_3O_4$/CNFs maintain a specific capacity of 395.6 mAh $g^{-1}$ after 100 cycles at a current density of 0.2 A $g^{-1}$. This is attributed to the synergistic effect between $FeTiO_3$ and $Fe_3O_4$, as well as the buffering effect of carbon fibers. These findings emphasize the critical influence of annealing conditions in tailoring the properties of the materials.

## CRediT authorship contribution statement

**Lisha Zhang:** Investigation, Writing – original draft, Formal analysis. **Fei Xie:** Formal analysis, Investigation. **Shujin Hao:** Formal analysis, Writing – review & editing. **Feiyu Diao:** Writing – review & editing, Formal analysis, Methodology. **Yiqian Wang:** Writing – review & editing, Funding acquisition, Supervision, Conceptualization.

## Declaration of competing interest

There are no conflicts to declare.

## Acknowledgments

The authors gratefully acknowledge the financial support from the High-end Foreign Experts Programs of the Ministry of Science and Technology, China (Grant Nos.: G2022025015L, G2022025016L), and Shandong Province “Double-Hundred Talent Plan” Program (Grant No.: WST2018006). Y. Q. Wang acknowledges the support from the Taishan Scholar Program of Shandong Province, China, the Qingdao International Center of Semiconductor Photoelectric Nanomaterials, and the Shandong Provincial University Key Laboratory of Optoelectrical Material Physics and Devices.

## Supplementary materials

Supplementary material associated with this article can be found, in the online version, at doi:10.1016/j.electacta.2025.146746.

## Data availability

Data will be made available on request.

## References

[1] F. Xie, M. Sun, X.L. Sheng, Q. Zhang, Z.B. Ling, S.J. Hao, F.Y. Diao, Y.Q. Wang, Graphene-wrapped $Fe_2TiO_5$ nanoparticles with enhanced performance as lithium-ion battery anode, Mater. Lett. 358 (2024) 135877.
[2] S. Li, J. Zhong, Z.B. Cui, Q. Zhang, M. Sun, Y.Q. Wang, Electron beam-induced morphology transformations of $Fe_2TiO_5$ nanoparticles, J. Mater. Chem. C 7 (2019) 13829–13838.
[3] X. Hou, X. Liu, H. Wang, X. Zhang, J. Zhou, M. Wang, Specific countermeasures to intrinsic capacity decline issues and future direction of $LiMn_2O_4$ cathode, Energy Storage Mater 57 (2023) 577–606.
[4] K.M. Min, K.S. Park, A.H. Lim, J.C. Kim, D.W. Kim, Synthesis of pseudo brookite-type $Fe_2TiO_5$ nanoparticles and their Li-ion electroactivity, Ceram. Int. 38 (2012) 6009–6013.
[5] X.J. Wang, X.J. Liu, G. Wang, Y. Xia, H. Wang, One-dimensional hybrid nanocomposite of high-density monodispersed $Fe_3O_4$ nanoparticles and carbon nanotubes for high-capacity storage of lithium and sodium, J. Mater. Chem. A 4 (2016) 18532–18542.
[6] Y.Q. Fu, Q.L. Wei, X.Y. Wang, G.X. Zhang, H.B. Shu, X.K. Yang, A.C. Tavares, S. H. Sun, A facile synthesis of $Fe_3O_4$ nanoparticles/graphene for high-performance lithium/sodium-ion batteries, RSC Adv. 6 (2016) 16624–16633.
[7] Y. Wang, X.M. Guo, Z.K. Wang, M.F. Lu, B. Wu, Y. Wang, C. Yan, A.H. Yuan, H. X. Yang, Controlled pyrolysis of MIL-88A to $Fe_2O_3$@C nanocomposites with varied morphologies and phases for advanced lithium storage, J. Mater. Chem. A 5 (2017) 25562–25573.
[8] R. Kang, W.Q. Zhu, S. Li, B.B. Zou, L.L. Wang, G.C. Li, X.H. Liu, D.H.L. Ng, J.X. Qiu, Y. Zhao, F. Qiao, J.B. Lian, $Fe_2TiO_5$ *nanochains as anode for high-performance lithium-ion capacitor*, Rare Met. 40 (2021) 2424–2431.
[9] S. Guo, Y. Wang, L. Chen, D. Pan, Z. Guo, S. Xia, Porous $TiO_2$-$FeTiO_3$@carbon nanocomposites as anode for high-performance lithium-ion batteries, J. Alloys Compd. 858 (2021) 157635.
[10] B. Naresh, K.G. Krishna, D. Rajasekhar, C. Kuchi, S.K. Kummara, P.S. Reddy, Synthesis and characterization of rGO wrapped 1-D NiO nanofibers for ammonia gas sensing application, Surf. Interfaces 40 (2023) 103012.
[11] J.J. Wang, X.L. Sheng, S.J. Hao, G.T. Liu, R.S. Cai, X.Y. Xue, Y.Q. Wang, Construction of $Fe_{0.64}Ni_{0.36}$@graphite nanoparticles *via* corrosion-like transformation from $NiFe_2O_4$ and surface graphitization in flexible carbon nanofibers to achieve strong wideband microwave absorption, J. Colloid. Interface Sci. 657 (2024) 193–207.
[12] X.L. Sheng, T. Li, M. Sun, G.J. Liu, Q.Y. Zhang, Z.B. Ling, S.W. Gao, F.Y. Diao, J. Z. Zhang, F. Rosei, Y.Q. Wang, Flexible electrospun iron compounds/carbon fibers: phase transformation and electrochemical properties, Electrochim. Acta 407 (2022) 139892.
[13] S.J. Hao, X.L. Sheng, F. Xie, M. Sun, F.Y. Diao, Y.Q. Wang, Electrospun carbon nanofibers embedded with heterostructured $NiFe_2O_4/Fe_{0.64}Ni_{0.36}$ nanoparticles as an anode for high-performance lithium-ion battery, J. Energy Storage 80 (2024) 110412.
[14] L. Wang, Y. Huang, X. Sun, H.J. Huang, P.B. Liu, M. Zong, Y. Wang, Synthesis and microwave absorption enhancement of graphene@$Fe_3O_4$@$SiO_2$@NiO nanosheet hierarchical structures, NANO 6 (2014) 3157–3164.
[15] L. Wang, N.T. Nguyen, X.J. Huang, P. Schmuki, Y.P. Bi, Hematite photoanodes: synergetic enhancement of light harvesting and charge management by sandwiched with $Fe_2TiO_5/Fe_2O_3$/Pt structures, Adv. Funct. Mater. 27 (2017) 1703527.
[16] Y.Q. Gao, Y.D. Li, G.Q. Yang, S.S. Li, N. Xiao, B.R. Xu, S. Liu, P. Qiu, S.J. Hao, L. Ge, $Fe_2TiO_5$ as an efficient co-catalyst to improve the photoelectrochemical water splitting performance of $BiVO_4$, ACS Appl. Mater. Interfaces 10 (2018) 39713–39722.
[17] M.C. Biesinger, L.W.M. Lau, A.R. Gerson, R.S.C. Smart, Resolving surface chemical states in XPS analysis of first row transition metals, oxides and hydroxides: *sc*, Ti, V, Cu and Zn, Appl. Surf. Sci. 257 (2010) 887–898.
[18] S. Rahimnejad, J.H. He, W. Chen, K. Wu, G.Q. Xu, Tuning the electronic and structural properties of $WO_3$ nanocrystals by varying transition metal tungstate precursors, RSC Adv. 4 (2014) 62423–62429.
[19] T.F. Li, J.F. He, B. Peña, C.P. Berlinguette, Curing $BiVO_4$ photoanodes with ultraviolet light enhances photoelectrocatalysis, Angew. Chem. Int. Ed. 55 (2016) 1769–1772.
[20] J.B. Chen, Z.Y. Li, Y.L. Ma, T. Sun, Visible light-driven $FeTiO_3/TiO_2$ composite materials for pollutant photodegradation, Chem. Lett. 45 (2016) 1319–1320.
[21] Y.S. Luo, J.S. Luo, J. Jiang, W.W. Zhou, H.P. Yang, X.Y. Qi, H. Zhang, H.J. Fan, D.Y. W. Yu, C.M. Li, T. Yu, Seed-assisted synthesis of highly ordered $TiO_2$@α-$Fe_2O_3$ core/shell arrays on carbon textiles for lithium-ion battery applications, Energy Environ. Sci. 5 (2012) 6559–6566.
[22] J.S. Luo, X.H. Xia, Y.S. Luo, C. Guan, J.L. Liu, X.Y. Qi, C.F. Ng, T. Yu, H. Zhang, H. J. Fan, Rationally designed hierarchical $TiO_2$@$Fe_2O_3$ hollow nanostructures for improved lithium ion storage, Adv. Energy Mater. 3 (2013) 737–743.
[23] S.M. Guo, S.Y. Wang, N.N. Wu, J.R. Liu, Y.X. Ni, W. Liu, Facile synthesis of porous $Fe_2TiO_5$ microparticulates serving as anode material with enhanced electrochemical performances, RSC Adv. 5 (2015) 103767–103775.
[24] A.S. Prakash, P. Manikandan, K. Ramesha, M. Sathiya, J.M. Tarascon, A.K. Shukla, Solution-combustion synthesized nanocrystalline $Li_4Ti_5O_{12}$ as high-rate performance Li-ion battery anode, Chem. Mater. 22 (2010) 2857–2863.
[25] D. Dambournet, I. Belharouak, K. Amine, $MLi_2Ti_6O_{14}$ (M = Sr, Ba, 2Na) lithium insertion titanate materials: a comparative study, Inorg. Chem. 49 (2010) 2822–2826.
[26] Q.C. Wu, R.L. Jiang, H.W. Liu, X.J. Li, D. Xie, Facile synthesis of core-shell porous $Fe_3O_4$@carbon microspheres with high lithium storage performance, C. R. Chim. 23 (2020) 279–289.
[27] F. Zhang, Y.B. Chen, Q.H. Tian, Preparation of an improved performance $FeTiO_3$-based lithium-ion battery anode, Synth. Met. 260 (2020) 116302.
[28] F.F. Lin, H.H. Song, S.Q. Tian, X.H. Chen, J.S. Zhou, F. Wang, $Fe_{1.5}Ti_{0.5}O_3$ nanoparticles as an anode material for lithium-ion batteries, Electrochim. Acta 83 (2012) 305–310.
[29] S.H. Li, X.H. Wang, Z.M. Shi, J. Wang, G.J. Ji, X. Yaer, High-performance lithium-ion storage of $FeTiO_3$ with morphology adjustment and niobium doping, Materials (Basel) 15 (2022) 6929.

[30] D.Y. Qu, Z.H. Sun, S.Y. Gan, L.F. Gao, Z.Q. Song, H.J. Kong, J.A. Xu, X.D. Dong, L. Niu, Two-dimensional $Fe_2O_3/TiO_2$ composite nanoplates with improved lithium storage properties as anodic materials for lithium-ion full cells, Chem. Electro. Chem. 7 (2020) 4963–4970.
[31] C.A. Velásquez, F.A. Vásquez, M. Alvarez-Láinez, A. Zapata-González, J. A. Calderón, Carbon nanofibers impregnated with $Fe_3O_4$ nanoparticles as a flexible and high-capacity negative electrode for lithium-ion batteries, J. Alloys Compd. 862 (2021) 158045.
[32] Y.N. Zhang, P. Dong, J.B. Zhao, X. Li, Y.J. Zhang, Simple solution-combustion synthesis of $Fe_2TiO_5$ nanomaterials with enhanced lithium storage properties, Ceram. Int. 45 (2019) 11382–11387.
[33] K.M. Min, K.S. Park, A.H. Lim, J.C. Kim, D.W. Kim, Synthesis of pseudobrookite-type $Fe_2TiO_5$ nanoparticles and their Li-ion electroactivity, Ceram. Int. 38 (2012) 6009–6013.
[34] M. Sun, X.L. Sheng, S.J. Li, Z.P. Cui, T. Li, Q.Y. Zhang, F. Xie, Y.Q. Wang, Construction of porous $CoTiO_3$ microrods with enhanced performance as lithium-ion battery anode, J. Alloys Compd. 926 (2022) 166809.
[35] B. Zhang, F. Xie, S.J. Hao, M. Sun, F.Y. Diao, R.S. Cai, Y.Q. Wang, Effect of annealing atmosphere on the phase composition and electrochemical properties of iron-oxide-based electrospun nanofibers, J. Energy Storage 124 (2025) 116851.
[36] Q.H. Wu, R.H. Xu, R.F. Zhao, X.E. Zhang, W.L. Li, G.W. Diao, M. Chen, Tube-in-tube composite nanofibers with high electrochemistry performance in energy storage applications, Energy Storage Mater 19 (2019) 69–79.
[37] C. Zhang, Q. Zhou, H. Wang, J. Liu, Y. Zhang, S. Wang, The effects of binders on the lithium storage of $Fe_3O_4$/NiO heterostructures, Ionics (Kiel) 29 (2023) 3573–3584.
[38] J.R. Deka, D. Saikia, Y.H. Lai, H.-M. Kao, Y.C. Yang, $Fe_3O_4$ nanoparticle-decorated bimodal porous carbon nanocomposite anode for high-performance lithium-ion batteries, Batteries 9 (2023) 482–502.
[39] M. Tu, C. Yang, R. Zhang, X. Kong, R. Jia, L. Yu, B. Xu, One-step engineering carbon supported magnetite nanoparticles composite in a submicron pomegranate configuration for superior lithium-ion storage, Materials (Basel) 16 (2023) 313–324.
[40] C.G. Han, C. Zhu, N. Sheng, Y. Aoki, H. Habazaki, T. Akiyama, A facile one-pot synthesis of $FeO_x$/carbon/graphene composites as superior anode materials for lithium-ion batteries, Electrochim. Acta 235 (2017) 88–97.